ISSN 1330-3651 (Print), ISSN 1848-6339 (Online) https://doi.org/10.17559/TV-20240328001434
Original scientific paper

# Optimization of the Cantilever Beam with TPMS Lattice Structure

Janko MOROSAVLJEVIĆ*, Dražan KOZAK, Ivan MOROSAVLJEVIĆ, Junfeng ZHAO

**Abstract:** The topology optimization has been presented in the example of a gyroid cantilever beam with a rectangular cross-section by using the software nTopology. The accuracy of the numerical model was checked by analytical solution, and by measuring strain in the printed beam. The direct integration method has been used to calculate deflection with the variation of the moment of inertia along the beam's axial axis. The corresponding stress and strain values were also calculated and compared with the numerical ones. The values are much lower since the effect of stress concentration has not been considered in analytical solutions. Experimental analysis by measuring strain with strain gauges on a 3D-printed beam was made to confirm the results. In the next step it was determined that the diamond type fits best according to the results of maximum deflection from the chosen three TPMS lattice structures. To optimize the topology of the beam, the thickness of the diamond cell was used as a parameter. The goal was to strengthen the structure by increasing the wall thickness of cells in the places where the beam has higher elastic stress values to get better stress distribution. The mass was additionally reduced by 16.35%.

**Keywords:** cantilever beam; lattice structure; nTopology; structural optimization

## 1 INTRODUCTION

The great interest of the public, and especially of scientists from various fields, enabled the significant development of 3D printing technology. Accordingly, ideas about printing different materials were developed, which, among other things, resulted in a wide range of different types of 3D printers (depending on the applied technology and material) and a wide range of applications. Simple manufacturing of structures with complex geometry offers the possibility of using porous, i.e., hollow structures of precisely determined, controlled geometry. Therefore, additive manufacturing enables the production of solid, light constructions made of complex lattice structures, the geometry that cannot be achieved by conventional production methods [1].

There are different categorizations of lattice structures, but the essential division for this article is the one that divides porous structures into lattice structures consisting of supports (Strut-based lattice structures) and lattice structures consisting of triply periodic minimal surfaces (TPMS) [2]. Strut-based lattice structures consist of supports interconnected in nodes, whose thickness, length, and orientation can be changed. The most common examples are body-centered cubic (BCC) and face-centered cubic (FCC) [3]. The second group of lattice structures is the triply periodic minimal surfaces, porous structures with zero mean curvature of the surface. TPMS are generated by algorithms and can be represented by mathematical Eq. (2).

The combination of lattice structure and additive manufacturing certainly represents a great discovery not only in the field of construction but also in the field of industrial product design. Many researchers are investigating properties and calculation approaches for such structures for their application. Since the porous structures produced by additive manufacturing have anisotropic elastic properties, there were investigations of the effect of pore distribution. According to Kowalczyk-Gajewska et al. [4], there is a non-negligible influence of morphological features on the developed anisotropy degree of the effective elastic stiffness of a porous material even if the solid phase is isotropic and pores are spherical. According to Marco et al. [5], each type of lattice cell has different mechanical properties, so there were investigations of several lattice and porous structures on what type to select based on their mechanical behaviour under different conditions and configurations using finite element models. Numerical models have been validated and compared with experiments extracted from literature, leading to accurate results. On the other hand, according to Carraturo et al. [6], a not negligible error occurs between as-built numerical and experimental results, possibly due to the non-homogeneous material distribution within lattice trusses.

The main emphasis of using lattice structures is to achieve a high strength-to-weight ratio by reducing the mass as much as possible. Therefore, lattice structures are used to optimize various kinds of structures. According to Liu et al. [7], topology optimization of functionally graded lattice structure considering structure buckling can greatly improve both the stability and stiffness of the optimal structure.

In most cases the stress and strain of the construction are not equally distributed, so to achieve an optimal structure, there is an approach to model the variable cellular structure according to Fryazinov et al. [8]. Therefore, in the places where the stress is minimal, there can be bigger cells, and in the places, where the stress is maximal, smaller cells. Based on that approach, the stress distribution in the construction will be more constant and the mass will be reduced.

Lattice structures are applied to various industries where mass is the main design objective in calculation. In the aerospace and automotive fields such design can lead to less fuel consumption and higher performance at the same time which is the main reason why the lattice structures have been adopted [9]. According to Mesicek et al. [10], the topological optimisation of the Formula Student bell crank was applied in order to accomplish weight reduction, and due to that, reduction of fuel consumption. Considering the possibilities of metallic 3D printing, they suggest that in the next research, they will apply the lattice structure to a design of bell crank to accomplish even higher mass decreasing. According to Hussain et al. [11], they investigated the utilization of octet

truss lattice structures in gas turbine blades to achieve weight reduction and improvement in vibration characteristics. Moreover, they concluded that such structure can be utilized in turbine blades to significantly reduce weight, stress level, and deformation along with an increasing first natural frequency.

By the cited literature, this article will analyze how lattice structures react to bending. The best practical example would be a cantilever beam with a rectangular cross-section because of its simplicity.

## 2 A POROUS BEAM DESIGN AND 3D PRINTING

The total analyzed beam length was 130 mm, and the height and width of the rectangular cross-section of the beam were 6 mm and 10 mm. One of the reasons for defining these dimensions is the dimension of the 3D printer's working area. Due to the experimental test, two holes were modelled at one of the ends of the beam, which was used to clamp the beam with the screws, while the other side was loaded with a transverse force. The screw holes have a diameter of 3 mm at a distance of 7 mm, while the distance between the first hole and the front of the beam is 3.5 mm. Given the size of the screw head, a 7 mm gap between the holes is sufficient to avoid overlap and secure fastening.

The beam is made of a porous structure consisting of Gyroid cells. The exceptions are the part with screw holes, the part where the strain gauge is intended to be placed, and the surface where the force is intended (3 × 3 × 1 mm). In order to achieve proper glue adhesion, the surface where the strain gauge is placed is filled with a 1 mm thick layer of full imprint material. A quadrilateral grid with the origin at the central axis of the console was chosen for the disposition of Gyroid cells. The thickness of each Gyroid cell is 1.8 mm. Frame with the gyroid cells was intersected with the initial model by the Boolean operator to get exactly the wanted dimension of the lattice structure. The initial model of the beam was created in the program package SolidWorks 2018 and then imported as the .stl file into the program package nTopology where the lattice structure was created. The quadrilateral grid with the origin at the central axis of the designed lattice cantilever beam is shown in Fig. 1.

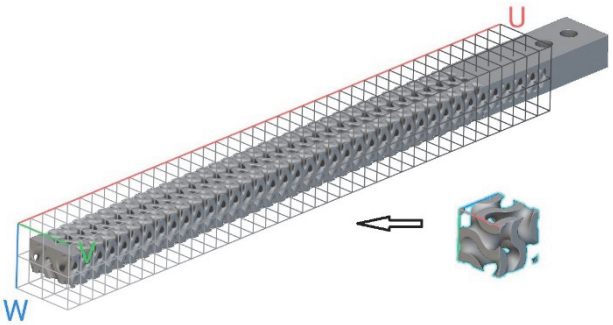


**Figure 1** Quadrilateral grid with the origin at the central axis of the designed lattice cantilever beam

The mass of the porous model is 23.07% lighter than the mass of the solid model. The mass, in addition to the dimensions of the beam and the characteristics of the material, is directly affected by the type of cell, the thickness of the cell walls, the density of the arrangement of cells, and their size. If the stress and deformation results are within the permissible limits, it is possible to reduce the mass even more by changing the specified parameters of the cell, which is the goal of the construction optimization process.

To perform the experimental analysis, with the aim of comparing the results obtained by analytical and numerical calculation, it was necessary to 3D print the specified porous beam. The used 3D printer to create the specimens was ENDER 3 PRO, and the chosen material was PLA. To calibrate the measuring instrument and, therefore, ensure valid measurement results, it was necessary to print a solid beam which was used for the calibration procedure of the tensometry instrument. The model, previously created in the nTopology, was exported in .stl format, which is a suitable format for importing into the Ultimaker Cura program package. In the software, the model was positioned on the working area of the 3D printer and the parameters of printing were defined. The printing parameters for both beams were set the same to ensure the same experimental conditions, and G code was generated with the same post-processor settings. Tab. 1 shows 3D printing parameters.

**Table 1** 3D printing parameters

| Parameters | Unit | Value |
|---|---|---|
| Bed temperature | °C | 60 |
| Print speed | mm/s | 50 |
| Nozzle diameter | mm | 0.4 |
| Nozzle temperature | °C | 200 |
| Layer height | mm | 0.12 |
| Infill pattern | - | Grid |
| Infill | % | 100 |
| Wall thickness | mm | 0.8 |
| Filament diameter | mm | 1.75 |
| Wall line count | - | 3 |

After printing the beams, it was necessary to make a base that would be rigid enough to ensure that base deformations would not interfere with the measuring accuracy. Printed beams are shown in Fig. 2.

**Figure 2** 3D-printed beams attached to a rigid base

## 3 ANALYTICAL, NUMERICAL AND EXPERIMENTAL ANALYSIS OF 3D PRINTED LATTICE CANTILEVER BEAM

### 3.1 Analytical Calculation of the Strength of a Beam with a Variable Value of the Moment of Inertia

For the defined shape and dimensions of the beam, an analytical calculation of the strength was made. The beam is loaded for bending in such a way that one end of the beam is clamped and the other one is loaded with force.

The stress during the bending of the structure can be determined for each cross-section of the structure while knowing the values of the bending moment and the moment of inertia of the cross-section.

Unlike a beam with a solid cross-section, for which the value of the moment of inertia is constant over the entire length, with a porous beam it is possible to change the density of the structure and thereby directly influence the values of the moment of inertia, and consequently also influence the stress values respectively. Moreover, it is possible to control the stress values in order to achieve a more even stress distribution which results in the reduced mass of the part and the final price of the used material which is an integral part of almost all requirements lists.

Parameters required for the calculation are force, length of the cantilever beam, modulus of elasticity, and moment of inertia of the cross-section. The parameters for the calculation are shown in Tab. 2.

**Table 2** Parameters for the calculation

| Parameters | Unit | Value |
|---|---|---|
| Loading force, $F$ | N | 0.98 |
| Young's modulus of elasticity, $E$ [12] | MPa | 1757 |
| Length of section AB, $L_1$ | mm | 15 |
| Length of section AC, $L$ | mm | 115 |

The boundary condition and loading of the beam with the diagram of transverse forces and moments are shown in Fig. 3 [13].

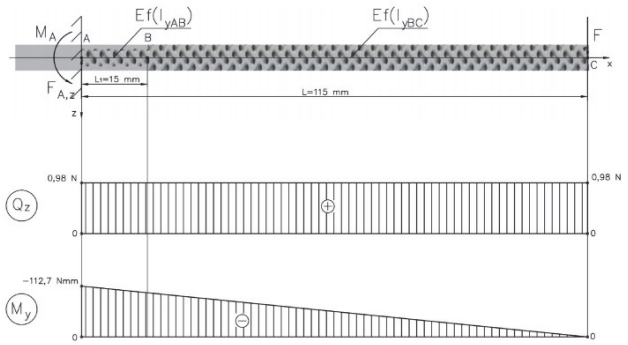


**Figure 3** Clamped and loaded cantilever beam with diagram of transverse forces and moments

Considering that the structure is porous and ununiform, the moment of inertia is not the same across the entire length of the beam, therefore it changes in accordance with the porosity/length function. Defining a function and solving differential equations with such a function would be overly complex and difficult. Therefore, to simplify, the moments of inertia are determined for every cross-section with the step of 0.1 mm along the length of the beam separately. The arrangement of the Gyroid cells within the cantilever volume is uniform which means that the moment of inertia values will be repeated after a certain distance.

The cantilever beam was divided according to the values of the moment of inertia into two parts: a part of the beam with a length of 15 mm covered with a 1 mm thick layer filled with the material on the top and bottom side, and a second entirely porous part of the beam. For this reason, the values of the moment of inertia are shown in two diagrams. The first diagram for values from point A to point B is shown in Fig. 4, and the second for values from point B to point C is shown in Fig. 5.

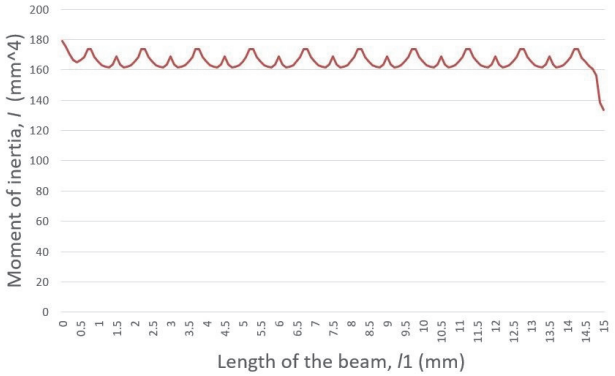


**Figure 4** Moment of inertia diagram for section AB of a porous cantilever beam

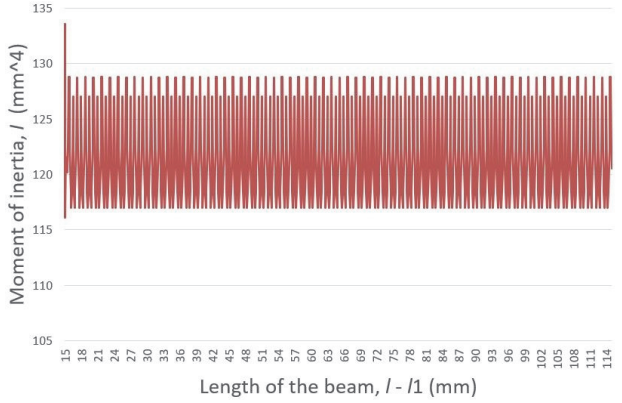


**Figure 5** Moment of inertia diagram for section BC of a porous cantilever beam

The direct integration analytical method was used to calculate the deflection and the slope of the beam [14]. The initial formula from which the slopes and deflections were obtained is:

$$\frac{\mathrm{d}^2 w}{\mathrm{d}x^2} = -\frac{M_y}{E \cdot I_y} \tag{1}$$

To solve the differential equation, it was necessary to determine a function of the bending moment rate change through the entire length of the beam [13].

$$M_y = -F \cdot L + F \cdot x \tag{2}$$

By integrating Eq. (1), the slope and the deflection functions were obtained for two parts of the beam, one from point A to point B, and the second from point B to point C.

$$\frac{dw_1}{dx} = -\frac{F \cdot L \cdot x - \frac{F \cdot x^2}{2} + C_1}{E \cdot I_{y\mathrm{AB}}} \tag{3}$$

$$\frac{dw_2}{dx} = -\frac{F \cdot L \cdot x - \frac{F \cdot x^2}{2} + C_3}{E \cdot I_{y\mathrm{BC}}} \tag{4}$$

$$w_1 = -\frac{\frac{F \cdot L \cdot x^2}{2} - \frac{F \cdot x^3}{6} + C_1 \cdot x + C_2}{E \cdot I_{yAB}} \quad (5)$$

$$w_2 = -\frac{\frac{F \cdot L \cdot x^2}{2} - \frac{F \cdot x^3}{6} + C_3 \cdot x + C_4}{E \cdot I_{yBC}} \quad (6)$$

It was also necessary to determine the expressions for the integration constants in order to include the boundary conditions. The following expressions represent the integration constants for the first part of the beam from point A to point B.

$$C_1 = \frac{\mathrm{d}w_1}{\mathrm{d}x} \cdot E \cdot I_{yAB} - F \cdot L \cdot x \cdot \frac{F \cdot x^2}{2} \quad (7)$$

$$C_2 = w_1 \cdot E \cdot I_{yAB} - \frac{F \cdot L \cdot x^2}{2} + \frac{F \cdot x^3}{6} - C_{1 \cdot x} \quad (8)$$

From the condition of continuity of the elastic line at point B, the value of slope and deflection on the left side is equal to values on the right side, so the integration constants $C_3$ and $C_4$ for part BC could be calculated.

$$C_3 = I_{yBC} \cdot \frac{F \cdot L \cdot x - F \cdot \frac{x^2}{2}}{I_{yAB}} + \frac{F \cdot x^2}{2} - F \cdot L \cdot x \quad (9)$$

$$C_4 = I_{yBC} \cdot \frac{F \cdot L \cdot \frac{x^2}{2} - F \cdot \frac{x^3}{6}}{I_{yAB}} - \frac{F \cdot L \cdot x^2}{2} + \frac{F \cdot x^3}{6} - C_3 \cdot x \quad (10)$$

A calculation was made for every 0.1 mm of beam length with new moment of inertia values. For every 0.1 mm of beam length, the calculated slope and deflection results from the previous step were set as a new boundary condition until the end of the beam was calculated. Therefore, each equation had different integration constants C and D, and the boundary conditions for the beginning of the calculation were defined in a way that in the clamping point, the deflection and slope are equal to zero.

To simplify and automate the analytical solution Excel MS was used. Eq. (3) to Eq. (10), and initial boundary conditions for $x$ = 0 mm, $w(0) = 0$ and $\mathrm{d}w/\mathrm{d}x\ (0) = 0$ were included in the calculation. It was also necessary to include the input parameters, the total length of the beam, the modulus of elasticity, and the force.

The deflection results are shown in Fig. 6. The maximum deflection value of 2.49 mm is in point C, which is expected for the cantilever beam. With regard to the positive direction of the $z$-axis from Fig. 3, the values of deflection in the diagram are shown as negative.

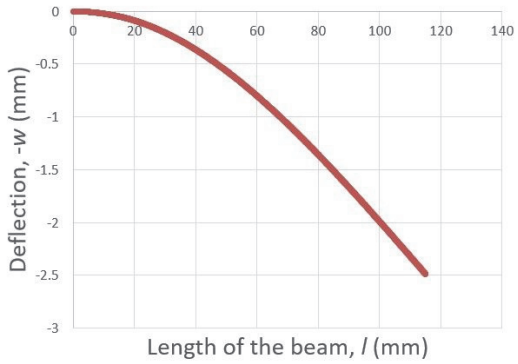


**Figure 6** The deflection line of the beam

To calculate the normal strain of the beam, the following equation was used which represents the dependence of the deflection of the beam on the normal strain for a uniaxial stress state.

$$\varepsilon = \frac{6 \cdot E \cdot I_y \cdot w - 6 \cdot C \cdot x - 6 \cdot D}{3 \cdot l \cdot x^2 - x^3} \cdot \frac{b \cdot l_d}{2 \cdot E \cdot I_y} \quad (11)$$

The calculation of the strain was made for every 0.1 mm of the length of the beam as in the previous calculation of deflection. The normal strain of the beam in dependence on its length is shown in Fig. 7.

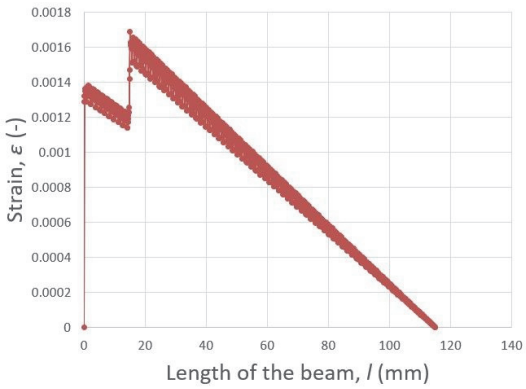


**Figure 7** Normal strain of the beam in dependence on its length

The normal stress in this case, since it is a uniaxial state of stress, was calculated according to the calculated values of normal strain of the beam using the following expression:

$$\sigma = E \cdot \varepsilon \quad (12)$$

Normal stress in the dependence on the length of a beam is shown in Fig. 8.

During the analytical calculation of deflection, normal stress, and strain, the stress concentrations expected at the edges of the Gyroid cells were not taken into account, and for this reason, deviation from the results obtained by numerical calculation is expected. Furthermore, to confirm the assumption of possible deviation, a numerical calculation had to be carried out.

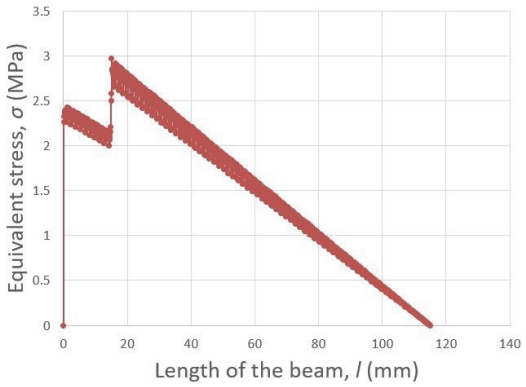


**Figure 8** Normal stress in the dependence on the length of a beam

### 3.2 Numerical Analysis of the Strength of a Beam in nTopology

In addition to modelling lattice structures, the nTopology software has the possibility of creating numerical calculations for given problems. The software utilizes the finite element method, which is one of the numerical methods based on the physical discretization of the continuum by dividing it into a grid of finite elements [15]. To optimize geometries with complex structures in traditional CAD software, such as lattice structures, the computer must have a lot of processing power to do so in some reasonable time. nTopology works with a different logic, and transforms the model into the implicit model, and makes it much easier for the computer to calculate.

For solving a problem, a mesh of tetrahedral elements with quadratic geometric order was used. The mesh consists of 1731750 elements and 2638355 nodes. The meshed model is shown in Fig. 9.

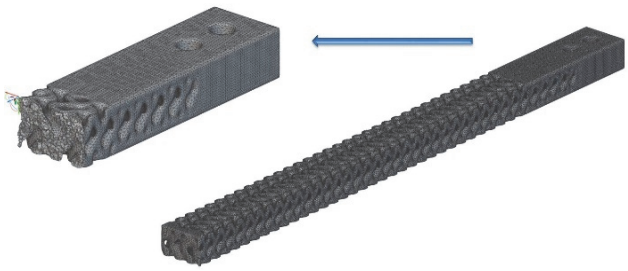

**Figure 9** Meshed model

The material was defined with the same Young's modulus of elasticity as in analytical calculation, except it was needed to include Poisson's ratio with the value of 0.42 and density of the material of $0.00124\ \mathrm{g\cdot mm^3}$ [16].

The force that loads the beam acts downwards ($-Y$ vertical axis direction) and amounts to 0.98 N. Considering the dimensions and material of the beam, the selected amount of force ensures that it remains in the elastic area of the sigma-epsilon diagram, and it is the same value as in the analytical calculation. Due to the clamping of the beam, on the surfaces inside the bore and on the surface that touches the rigid base for experimental measurement, immovable supports are placed, which, in addition to preventing movements in the direction of all three axes, also prevent rotations around them. Defined boundary conditions and loads are shown in Fig. 10.

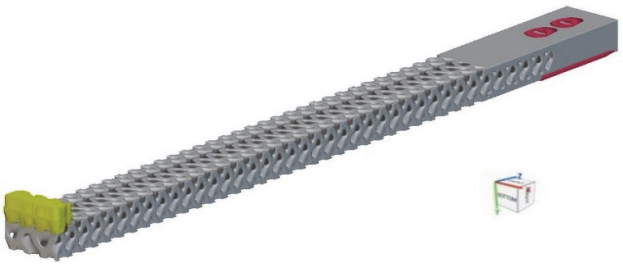

**Figure 10** Boundary conditions and loading

Processor Intel Core i9-13900K was used for the simulation and roughly the computing time of the simulation was 3 minutes. The results of normal stress are shown in Fig. 11 and Fig. 12 and the results of total deformation of the modeled beam are shown in Fig. 13.

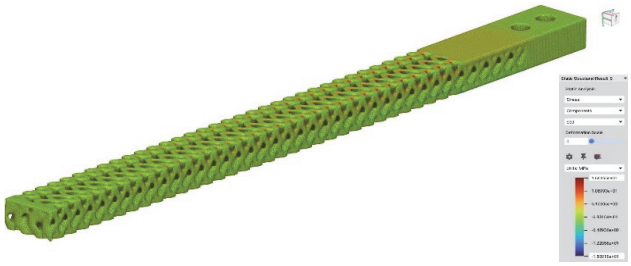

**Figure 11** Normal stress results

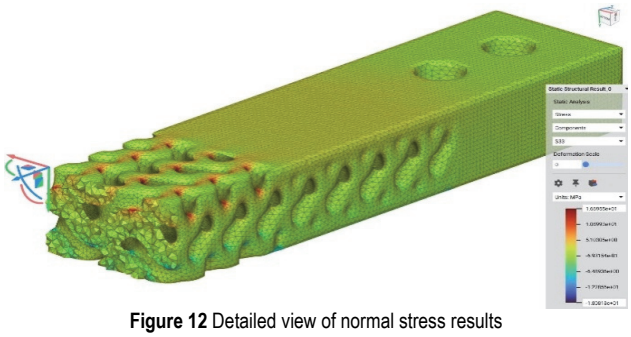

**Figure 12** Detailed view of normal stress results

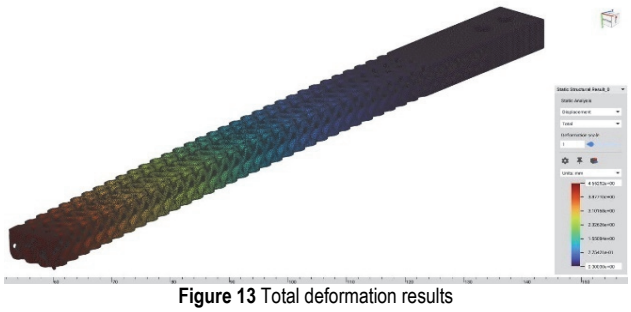

**Figure 13** Total deformation results

The differences between the results in analytical and numerical calculation for the force of 0.98 N and immovable support placed on the end of the beam are shown in Tab. 3.

**Table 3** Analytical and numerical calculation results

| Analytical calculation | Numerical calculation |
|---|---|
| Maximum deflection, $w$ / mm | |
| 2.49 | 4.65 |
| Maximum normal stress, $\sigma$ /MPa | |
| 2.97 | 18.08 |
| Maximum normal strain, $\varepsilon$ / - | |
| 0.0017 | 0.0084 |

Comparing the obtained numerical and analytical results, there are substantial differences in the values of maximum deflection, maximum normal stress, and maximum normal strain. Therefore, the analytical calculation that was made is declared unsuitable for modeling such a complex structure. It is possible that the differences occurred because a stress concentration was not used in consideration within an analytical calculation since there is no viable method for such a complex structure.

### 3.3 Experimental Analysis of 3D Printed Lattice Cantilever Beam

Experimental analysis was needed to confirm the numerical results and it was carried out by measuring the strain using a strain gauge. To measure the strain, a device with a strain gauge, Arduino microcontroller, and AD converter were used [17, 18]. A strain gauge was glued to measure the strain on the length of 7 mm from the fixed support. Deforming a specimen results in a change of the gauge resistance and, therefore, the read voltage on the AD converter. AD converter converts the read change values into digital form. Obtained digital data by the AD converter is processed by the microcontroller and sent to the computer. The computer processes the data according to the written code and displays the measurement results. The measuring device is shown in Fig. 14.

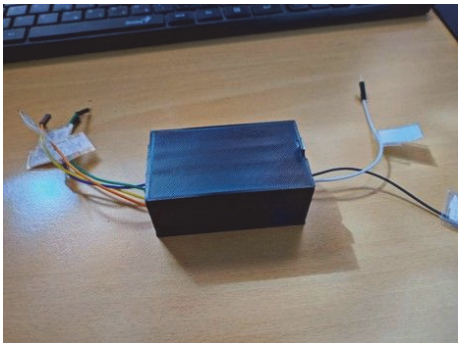

**Figure 14** Measuring device

For calibration, it was necessary to make an analytical calculation of the strain on the point where the strain gauge is glued ($L_2$ = 7 mm). Calibration of the device was carried out on the 3D-printed cantilever beam with a full solid rectangular cross-section because it is possible to obtain an accurate analytical calculation as a calibration reference. The dependence of suspended weight on the beam and strain is shown in the following expression.

$$\varepsilon_D = \frac{6 \cdot g \cdot l_2}{E \cdot a \cdot b^2} \cdot m \tag{13}$$

The values $a$ and $b$ are the width and height of the full cross-section of the beam. The results of analytical calculation for different suspended weights on the beam are shown in Tab. 4.

Once the strain values were known for different suspended weights, values of each load were read and recorded, respectively. The average of the read values by the program for each load case was equated with the analytically calculated strain value. For the six load cases listed in Tab. 4, and for the case when the sample is unloaded, the measurement results are shown diagrammatically in Fig. 15.

**Table 4** Analytical calculation for different suspended weights on the full solid rectangular cross-section beam

| Strain, $\varepsilon$ / - | Mass, $m$ / g |
|---|---|
| 0.0005164 | 82.3 |
| 0.0006714 | 107 |
| 0.001188 | 189.3 |
| 0.001380 | 220 |
| 0.002052 | 327 |
| 0.002568 | 409.3 |

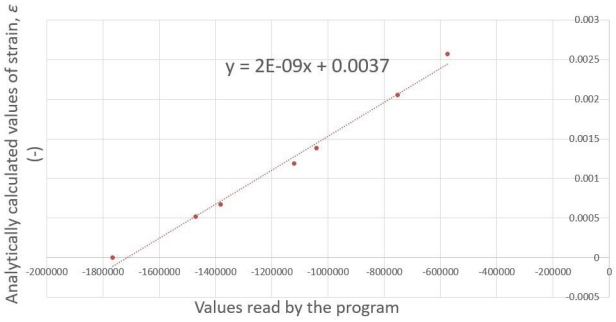


**Figure 15** Values read by the program and analytically calculated values of strains

A linear function of the strain in relation to the given loads was obtained, which confirms that the beam is in the elastic region. The determined function was written in the program code. The measurement of strain of a porous beam is shown in Fig. 16.

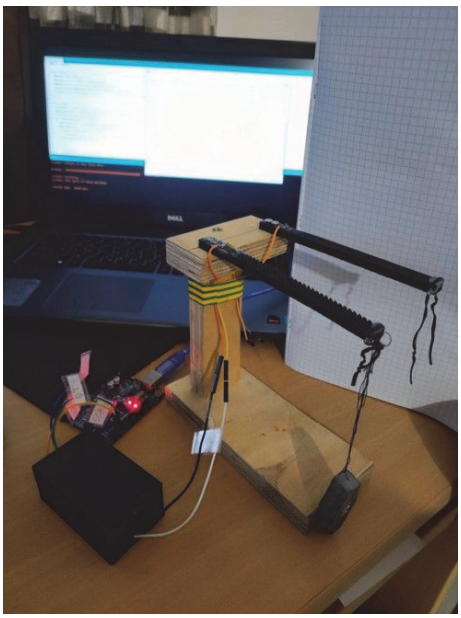

**Figure 16** The measurement of strain of a porous beam

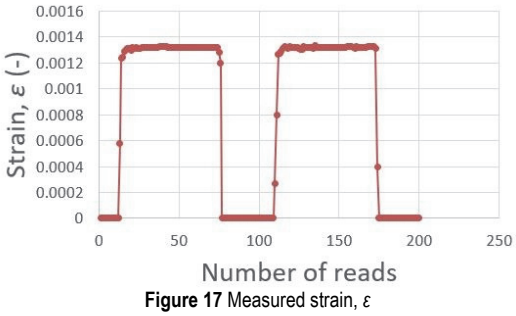


**Figure 17** Measured strain, $\varepsilon$

In order to ensure valid results, a measurement procedure was carried out twice with a mass of 100 g. The obtained results are shown in Fig. 17.

Since strain is entirely within the elastic region because of the magnitude of the applied load, the stress curve was obtained with Eq. (12). The calculated equivalent stress curve based on the strain results is shown in Fig. 18.

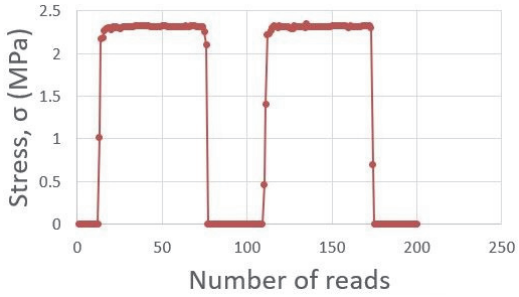


**Figure 18** Equivalent stress, σ

The measured strain average is $\varepsilon = 0.0013$ and the average equivalent stress is $\sigma = 2.27$ MPa. The value of maximum deflection was obtained by a vernier caliper. The measured maximum deflection is 4.4 mm. The difference between results from the numerical calculation and experimental analysis is shown in Tab. 4.

**Table 4** Numerical and experimental results

| Experimental analysis | Numerical calculation |
|---|---|
| Maximum deflection, $w$ / mm | |
| 4.4 | 4.65 |
| Calculated equivalent stress based on measured strain and numerical result at the same point of the beam, $\sigma$ / MPa | |
| 2.27 | 2.00 |
| Measured strain and numerical result at the same point of the beam, $\varepsilon$ / - | |
| 0.0013 | 0.0012 |

The obtained numerical results appear to be correct because experimental results are nearly identical. Insignificant deviations in obtained results are possibly due to imprecise positioning of the strain gauge and deviations in the mass of the weight. Also, there can be minor differences in the resistance of the Wheatstone bridge built in the device, but for this purpose, it is enough close to confirm numerical results. Stress concentrations on a lattice structure significantly affect the error of the analytical method, therefore further research is required to propose a modified method that would include correction factors to be considered for each type of the lattice structure or stress concentration calculation procedure.

## 4 OPTIMIZATION OF THE CANTILEVER BEAM WITH nTOPOLOGY SOFTWARE

### 4.1 Lattice Type of Cell as a Parameter for Optimization

Since the Gyroid belongs to the TPMS (Triply Periodic Minimal Surfaces) lattice structure type, for a better comparison of the results, Schwarz and Diamond types were selected for optimization since they also fall into that category. Hence, those three types were taken as a parameter in the calculation.

To make all the calculations for different structures of the beam, nTopology offers the possibility to make custom blocks in another file which are imported to the main working file. Later, in imported custom blocks it is possible to place the scalar list of values for the chosen variable and make the automated calculation for all of them at once.

It was required to create more geometries with diverse types of cells. The optimization parameter that enables to change in the porosity of the defined geometries was the wall thickness. The custom block was made which can generate automatically as many structures as needed by defining the inputs and outputs of the function. The scalar list with the values of the approximate thickness of the wall is imported and the geometries are automatically generated. The geometries with the Gyroid, Diamond, and Schwarz type of lattice are shown in Fig. 19, Fig. 20, and Fig. 21.

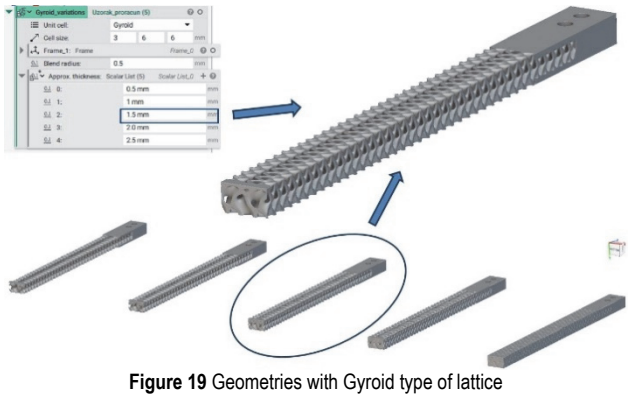

**Figure 19** Geometries with Gyroid type of lattice

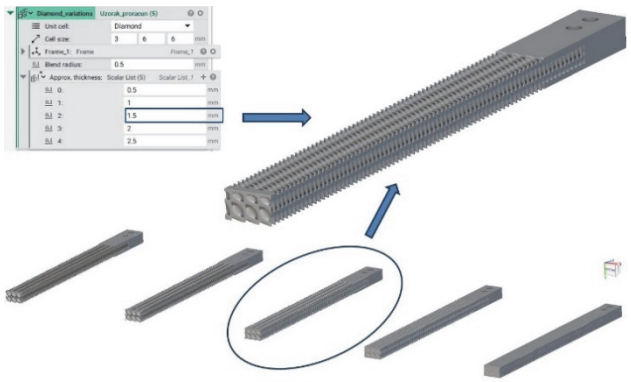

**Figure 20** Geometries with Diamond type of lattice

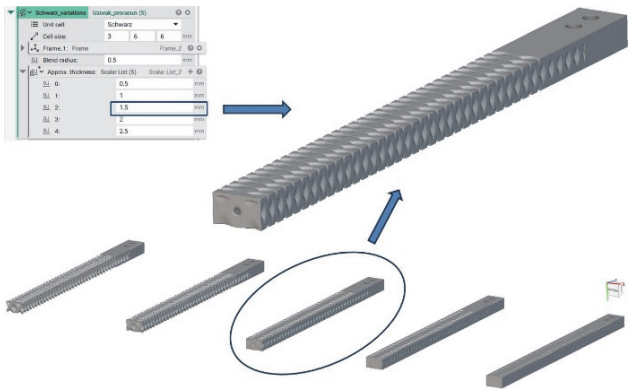

**Figure 21** Geometries with Schwarz type of lattice

After generating all the geometries, FEM analysis was used for each generated geometry, respectively. The custom block was made as a tool to calculate all geometries at once. Boundary conditions, mesh configurations, and the

material were the same as previously described in numerical calculation.

As a result of the made custom block, for each previously shown structure of every type of the cell, the results of equivalent stress and deflection of the beam were calculated. Each result can be found, singled out, and analyzed in the properties section in the list element function. To keep the calculation automated, the custom blocks for the stress probe and deflection probe were created to obtain results comparison for each type of the cell graphically and numerically, respectively. The probe point for equivalent stress for each structure is defined on the place where the strain gauge is glued. The probe point for maximum deflection is defined as the scalar value of the vector on the y-axis at the end of the beam.

To define the porosity of each beam, nTopology has the Preprogrammed block "Weight savings" which calculates how much weight compared to the full body of the beam is reduced (shown in percentage). The volume ratio *Vr* is opposite to weight savings, so it is described as 100% minus weight savings. The comparison of lattice-type structures based on the calculated equivalent stress is shown in Fig. 22.

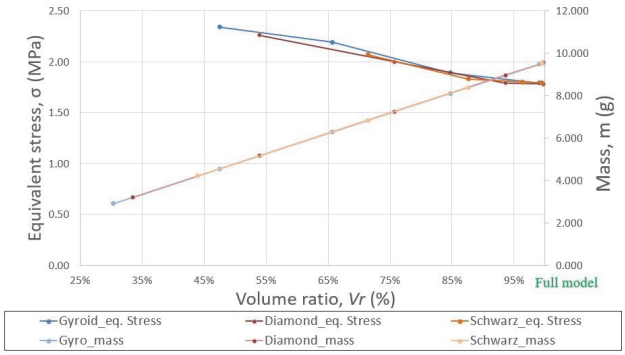


**Figure 22** The comparison of lattice-type structures based on the calculated equivalent stress

Since the values of the equivalent stress (Von Mises) are low, there is not a noticeable difference between each type of used cell. For lower *Vr*, Diamond, and Schwarz have also slightly lower equivalent stress, which means that they are a better choice in the view of equivalent stress than Gyroid. The comparison of lattice-type structures based on the calculated maximum deflection is shown in Fig. 23.

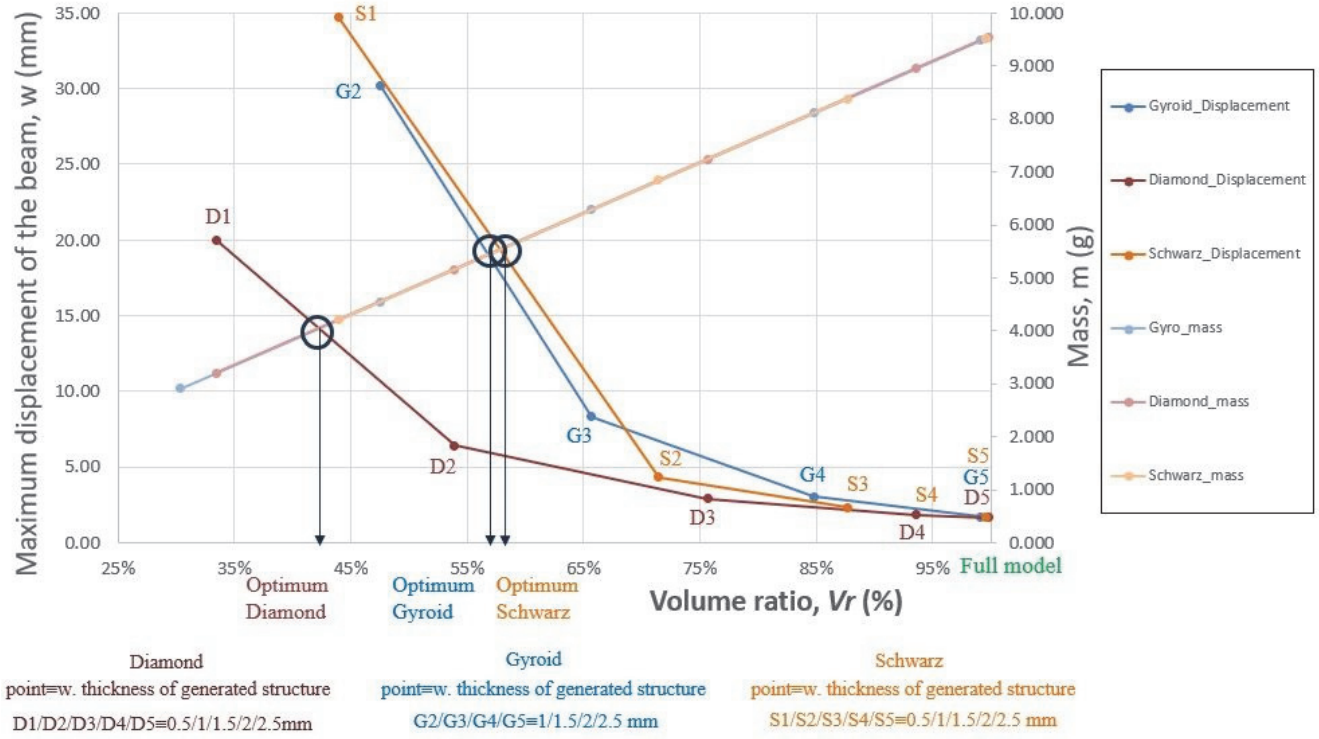


**Figure 23** The comparison of lattice-type structures based on the calculated maximum deflection

The Diamond structure has the optimal value with lower values of *Vr* than Gyroid and Schwarz and later lower values of maximum deflection with higher *Vr*. This is why Diamond would be the best choice to choose for the lattice type in this case.

### 4.2 Functional Graded Topology Optimization

The cantilever beam created with a Diamond structure with constant cell thickness between 0.5 mm and 1 mm gives the best results for deflection, but this solution makes sense for the structures where the uniform unit cell order is needed. However, in some cases, like for implants produced from biocompatible materials the mass could be even more reduced with better stress distribution along the length of the beam by changing the thickness of the cells in some range according to the stress field distribution.

For this example, to analyse how changing the wall thickness of the cells along the length of the beam can affect the results, the same frame for lattice cells and the same size of the unit cell were kept. Therefore, the parameter of optimization was the changeable thickness of Diamond cells along the length of the beam depending on the equivalent stress distribution results for a full cross-section of the beam.

To determine the scalar field with values of equivalent stress for the cantilever beam with a full rectangle cross-section as the input for optimization, the static analysis was made with the same boundaries as previously determined for the calculated gyroid lattice beam.

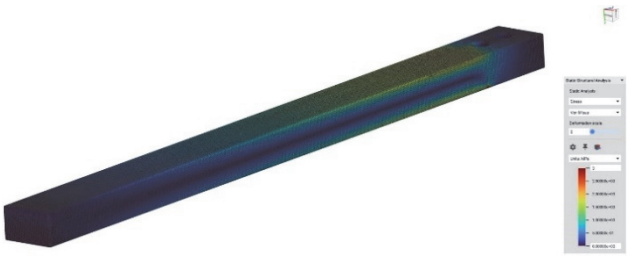

**Figure 24** Distribution of equivalent stress as input for optimization

According to the distribution of equivalent stress along the beam shown in Fig. 24, a structure was strengthened with the higher values of thickness of cells in the places where the beam has higher values of equivalent stress. With regard to the literature [12], the maximum tensile strength of the 3D printed PLA for this case is 62.4 MPa. For the optimization boundaries of the equivalent stress, the value around 5% of the maximum value of tensile stress was taken to keep the similar maximum deflection of the beam from previous calculations, and the equivalent stress is kept in the elastic field. The determined values of the thickness of diamond cells for the optimization boundaries were a minimum value of 1 mm and a maximum value of 4 mm. The optimized geometry of the beam is shown in Fig. 25.

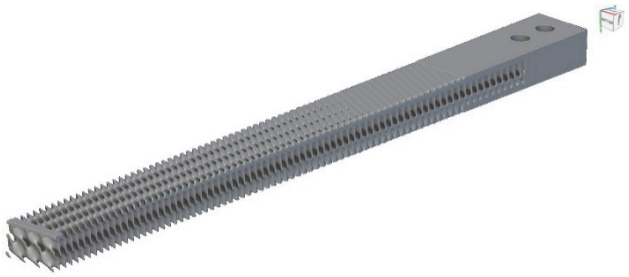

**Figure 25** The optimized geometry of the beam

As a result of functionally graded topology optimization, the geometry has changeable values of thickness of the cells along the beam from the values of 1 mm to 4 mm according to the distribution of equivalent stress for full body beam. The results of equivalent stress according to the Von Mises criterion are shown in Fig. 26 and Fig. 27.

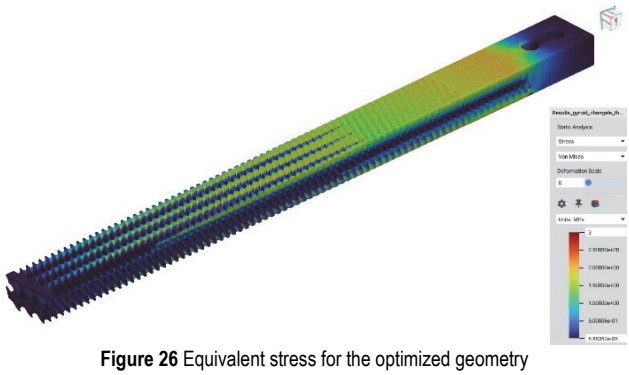

**Figure 26** Equivalent stress for the optimized geometry

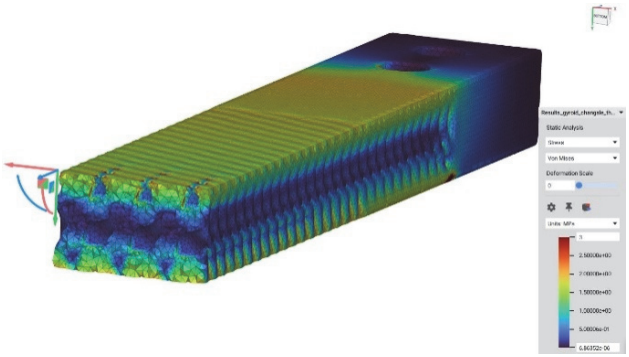

**Figure 27** Cross-section of the beam with equivalent stress results

According to the results of equivalent stress, it was concluded that it was within the defined boundaries and that it was optimized evenly along the length of the beam.

By comparing the values of the maximum deflection of the beam for the case before optimization (2.12 mm) and after (2.19 mm), it was concluded that the deflection results are nearly identical. Since the mass was reduced by an additional 16.35% and equivalent stress is within defined boundaries, the optimization was considered successful.

## 5 CONCLUSION

Comparing the obtained results, it can be concluded that the numerical and experimental results are nearly identical with insignificant deviation and analytical results are significantly different. Therefore, the analytical calculation that was made is declared unsuitable for modeling such a complex structure. In analytical calculation, a stress concentration was not used in consideration since there is no viable method to include it for such a complex structure. A possible solution to include stress concentrations in the analytical calculation would be to approximate the geometry with a value of the moment of inertia to a full body beam with a circular cross-section where the diameter is taken as a parameter. Then, it is possible to define the concentration factor from the literature for the transition of the diameter value.

If just one parameter is taken for optimization of lattice structures, it could make noticeable savings in the mass and much better stress distribution in the part. To generate and produce the lattice structure, it is particularly important to perform the optimization. The type of lattice cells should not be chosen solely by its appearance. Each type of lattice cell offers diverse kinds of mechanical properties that could be utilized depending on chosen boundary conditions and loading. To determine the type of cell that is the best for the application, it is necessary to conduct the optimization, as previously shown in this article, since it was concluded that the results can greatly vary.

As a result of functionally graded topology optimization, the optimized geometry has a 28.32% lighter mass in comparison to the initial model. Moreover, the mass was reduced by an additional 16.35% compared to the model with the constant wall thickness of 1.8 mm.

## 6 REFERENCES

[1] Maconachie, T., Leary, M., Lozanovski, B., Zhang, X., Qian M., Faruque, O., & Brandt, M. (2019). SLM lattice structures: Properties, performance, applications and

challenges. *Materials & Design, 183*, 108137. https://doi.org/10.1016/j.matdes.2019.108137
[2] Riva, L., Ceretti, E., & Ginestra, P. S. (2021). Mechanical characterization and properties of laser-based powder bed-fused lattice structures: a review. *The International Journal of Advanced Manufacturing Tehnology, 113*, 649-671. https://doi.org/10.1007/s00170-021-06631-4
[3] Echeta, I., Feng, X., Dutton, B., Leach, R., & Piano, S. (2020). Review of defects in lattice structures manufactured by powder bed fusion. *The International Journal of Advanced Manufacturing Tehnology, 106*, 2649-2668. https://doi.org/10.1007/s00170-019-04753-4
[4] Kowalczyk-Gajewska, K., Maj, M., Bieniek, K., Majewski, M., Opiela, K. C., & Zieliński, T. G. (2024). Cubic elasticity of porous materials produced by additive manufacturing: experimental analyses, numerical and mean-field modelling. *Archives of Civil and Mechanical Engineering, 24*, 34. https://doi.org/10.1007/s43452-023-00843-z
[5] Marco, M., Belda, R., Henar Miguélez, M., & Giner, E. (2021). Numerical analysis of mechanical behaviour of lattice and porous structures. *Composite Structures, 261*, 113292-113307. https://doi.org/10.1016/j.compstruct.2020.113292
[6] Carraturo, M., Alaimo, G., Marconi, S., Negrello, E., Sgambitterra, E., Maletta, C., Reali, A., & Auricchio, F. (2021). Experimental and Numerical Evaluation of Mechanical Properties of 3D-Printed Stainless Steel 316L Lattice Structures. *Journal of Materials Engineering and Performance, 30*, 5247-5251. https://doi.org/10.1007/s11665-021-05737-w
[7] Liu, L., Yi, B., Wang, T., Li, Z., Zhang, J., & Yoon, G. H. (2021). Investigation on numerical analysis and mechanics experiments for topology optimization of functionally graded lattice structure. *Additive Manufacturing, 47*, 102275. https://doi.org/10.1016/j.addma.2021.102275
[8] Fryazinov, O., Vilbrandt, T., & Pasko, A. (2013). Multi-scale space-variant FRep cellular structures. *Computer-Aided Design, 45*(1), 26-34. https://doi.org/10.1016/j.cad.2011.09.007
[9] Tao, W. & Leu, M. C. (2016). Design of lattice structure for additive manufacturing. *2016 International Symposium on Flexible Automation (ISFA)*, 325-332. https://doi.org/10.1109/ISFA.2016.7790182
[10] Mesicek, J., Pagac, M., Petru, J., Novak, P., Hajnys J., & Kutiova, K. (2019).Topological optimization of the formula student bell crank. *MM Science journal*, 2964-2968. https://doi.org/10.17973/MMSJ.2019_10_201893
[11] Hussain, S., Ghopa, W. A. W., Singh, S. S. K., Azman, A. H., & Abdullah, S. (2022). Experimental and Numerical Vibration Analysis of Octet-Truss-Lattice-Based Gas Turbine Blades. *Metals 2022, 12*(2), 340. https://doi.org/10.3390/met12020340
[12] Chacón, J. M., Caminero, M. A., García-Plaza, E., & Núñez, P. J. (2017). Additive manufacturing of PLA structures using fused deposition modelling: effect of process parameters on mechanical properties and their optimal selection. *Materials & Design, 124*, 143-157. https://doi.org/10.1016/j.matdes.2017.03.065
[13] Matejiček, F., Semenski, D., & Vnučec, Z. (2012). *Uvod u statiku sa zbirkom zadatka*. ISBN: 978-953-6048-68-7
[14] Alfirević, I. (1995). *Nauka o čvrstoći 1*. ISBN: 953-172-010-X
[15] Hrnjica, B. (2022). *Metoda konačnih elemenata*. ISBN: 978-9958-533-25-9
[16] Abidin, Z., Fadhlurrahman, I. G., Akbar, I., Putra, R. U., Prakoso, A. T., Kadir, M. Z., Astuti, A., Syahrom, A., Ammarullah, M. I., Jamari, J., & Basri, H. (2022). Numerical Investigation of the Mechanical Properties of 3D Printed PLA Scaffold. *Atlantis Highlights in Engineering, 9. Proceedings of the 5th FIRST T1 T2 2021 International Conference (FIRST-T1-T2 2021))*, 83-89. https://doi.org/10.2991/ahe.k.220205.015
[17] Raguž, I., Kozak, D., Crnogorac, K., & Hercog, M. (2018). Designing and Calibration of the System for Remote Strain Control. *2018 International Conference on Smart Systems and Technologies (SST)*, 73-79. https://doi.org/10.1109/SST.2018.8564706
[18] Morosavljević, I., Kozak, D., Morosavljević, J., & Opačak, I. (2022). Numerical and experimental analysis of the application of traditional woodworking joinery on 3D printed parts. *Proceedings of the 10th International Scientific and Expert Conference TEAM 2022*, 241-248.

**Contact information:**

**Janko MOROSAVLJEVIĆ**, mag. ing. mech., PhD student
(Corresponding author)
Mechanical Engineering Faculty in Slavonski Brod,
University of Slavonski Brod,
Trg Ivane Brlić Mažuranić 2, 35000 Slavonski Brod, Croatia
E-mail: jmorosavljevic@unisb.hr

**Dražan KOZAK**, Full Professor tenure, PhD
Mechanical Engineering Faculty in Slavonski Brod,
University of Slavonski Brod,
Trg Ivane Brlić Mažuranić 2, 35000 Slavonski Brod, Croatia
E-mail: dkozak@unisb.hr

**Ivan MOROSAVLJEVIĆ**, mag. ing. mech., PhD student
Mechanical Engineering Faculty in Slavonski Brod,
University of Slavonski Brod,
Trg Ivane Brlić Mažuranić 2, 35000 Slavonski Brod, Croatia
E-mail: imorosavljevic@unisb.hr

**Junfeng ZHAO**, Assistant Professor, PhD
School of Mathematics and Statistics,
Northwestern Polytechnical University,
Xi'an 710071, P.R. China
E-mail: zhaojf@nwpu.edu.cn